JOURNAL OF PROPULSION AND POWER
Vol. 23, No. 2, March–April 2007

Experimental Study of Near-Field Flow Structure in Hollow Cone Pressure Swirl Sprays

J. L. Santolaya, L. A. Aísa, E. Calvo, I. García, and L. M. Cerecedo
Zaragoza University, 50015 Zaragoza, Spain

DOI: 10.2514/1.20713

In this work the near field of the sprays resulting from the breakup of conical liquid sheets was investigated through experimental techniques. The dispersed and continuous phase velocities and the size of droplets were measured using a phase Doppler particle analyzer. A data postprocessing, applying the generalized integral method, was used to evaluate droplet volume fluxes and total liquid flow rates. The parameters of radial mean spread and spatial dispersion of the sprays were calculated and the overall droplet size distributions across the sprays were obtained. Two sheet disintegration regimes, perforations and surface wave instabilities, were analyzed. Measurements showed a significant increase in the atomization quality as well as in the liquid radial dispersion parameter for the wavy sheet disintegration. In addition, the effects of the collision phenomena on the droplet size distributions were shown. High collision rates were predicted in the spray densest zones and some collision outcomes, as the droplet coalescence or the separation with satellite droplet formation, were detected.

Nomenclature

A_o	=	atomizer orifice cross-sectional area
C_D	=	atomizer discharge coefficient
D	=	droplet diameter
D_{V50}	=	smaller droplet diameter that includes 50% of the total liquid volumetric flow rate
d_o	=	atomizer orifice diameter
def	=	liquid flow rate deficits
F_{ac}	=	cumulative liquid flow rate
F_T	=	total liquid volumetric flow rate
$\boldsymbol{f}_V$	=	droplet volume flux
P	=	injection pressure
N	=	droplet number
N_{cl}	=	total number of droplet size classes
Q	=	injected liquid volumetric flow rate
R_{50}	=	radial mean spread of the spray
Re	=	Reynolds number
r	=	radial coordinate
r^*	=	dimensionless radial coordinate
S	=	span of the cumulative distribution
S_T	=	spray cross-transversal area
tt	=	droplet transit time through the PDPA detection volume
$\boldsymbol{V}$	=	velocity vector
$\bar{V}$	=	mean velocity
Vol	=	droplet detection volume
We	=	Weber number
x	=	axial coordinate
ΔR	=	radial dispersion of the spray
Δt	=	measurement time at each location

Subscripts

a	=	air
D	=	droplet
i	=	droplet size class
j	=	class of droplet velocity modules
k	=	class of droplet velocity directions
max	=	maximum value
r	=	radial component
x	=	axial component

Received 24 October 2005; revision received 27 July 2006; accepted for publication 11 August 2006.

Introduction

PRESSURE swirl atomizers (PSN) are found in many engineering applications such as the energy and power industries, due to their good atomization characteristics and their geometrical simplicity. The operation of these injectors is based on the high angular momentum that acquires the fluid inside the atomizer. As a result, the liquid concentrates along the walls at the same time as an air core develops around the axis of symmetry. Previous studies [1,2] have analyzed experimentally and theoretically the characteristics of this complex internal flow.

The liquid, forced to follow a helical path, emerges from the nozzle in the form of a hollow conical sheet that soon becomes unstable and disintegrates because of different mechanisms. The breakup phenomenon has been extensively studied, particularly in plane configurations. For conical sheets generated by PSN, Lefebvre [3] observed that a collapsed tulip-shape sheet changed to a diverging wavy sheet as the liquid injection pressure was increased. The effect of fluid properties on the sheet characteristics was also examined through experimental methods [4,5]. It was demonstrated that an increase on the viscosity or on the surface tension of the liquid injected inhibits the growth of surface waves as breakup mechanism and generates more developed sheets.

The mean size and spatial distribution of the droplets resulting from the liquid disintegration do not depend only on the sheet breakup process. The drop-drop collision phenomena and the two-way coupling between the phases (air-droplet) affect specially to the formation of the initial spray structure.

The interaction of the spray with the air flowfield redistributes spatially spray droplets due to the differences in droplet inertia, momentum, and drag. Typically, for pressure atomizers in the absence of any significant external air flowfield, small droplets couple to the local induced airflow whereas larger droplets tend to maintain the higher velocity of the liquid sheet [6]. On the other hand, it is well known that the air entrainment has a decisive influence on the heat and mass transfer between phases and therefore on the combustion efficiency. However, entrained airflow rate measurements [7] are relatively little.

Droplet collision is expected to be a frequent event immediately downstream of the sheet breakup, promoted by the high concentrations and by the relative velocities of the droplets. In a previous investigation, Qian and Law [8] establish five distinct

Table 1 Oil properties at $T = 95°C$

Density	$\rho_l = 847$ Kg/m^3
Dynamic viscosity	$\mu_l = 0.0166$ Kg/ms
Surface tension	$\sigma_l = 0.032$ N/m
Vapor pressure	$P_v = 98.13$ Pa
Refractive index	$m = 1.483 + 0.00072i$

regimes of collision outcomes, depending on the liquid and gas properties, the impact conditions and the droplet sizes. In general, the droplets may experience bouncing, stable coalescence or temporary coalescence followed by disruption or fragmentation. Between these outcomes, stable coalescence and fragmentation can significantly modify the droplet size distribution as spray develops.

Many researchers detected the increase of the droplet mean diameter along the spray distance. Rüger et al. [9], using numerical tools for the spray prediction, revealed that this is mainly due to drop coalescence.

Technological advances available for spray measurements, as phase Doppler interferometry, have enabled the characterization of pressure swirl spray structures in detail. However, most experimental investigations [9–11] were focused on the analysis of the spray far field and in general for an unique sheet disintegration regime. The present work aims at studying the spray near field for different sheet disintegration regimes. Measuring difficulties arise at this region due to the high liquid density, and inaccuracies of the liquid flow rate evaluation can be important. Emphasis is laid on the determination and analysis of the local and global droplet size distributions. The related measurements can provide appropriate inlet conditions for the validation and development of numerical models in further investigations.

Experimental Setup

Experiments were performed at a specially designed facility for spray generation under controlled conditions. The test liquid was oil of industrial origin, used previously in lubrication and refrigeration applications. The oil properties measured at the injection temperature are listed in Table 1.

The liquid was driven from the tank to the nozzle through a pumping line (see Fig. 1). The oil was filtered to eliminate the undesirable solid particles and was heated by an electrical resistance to decrease its high viscosity and to improve atomization performance.

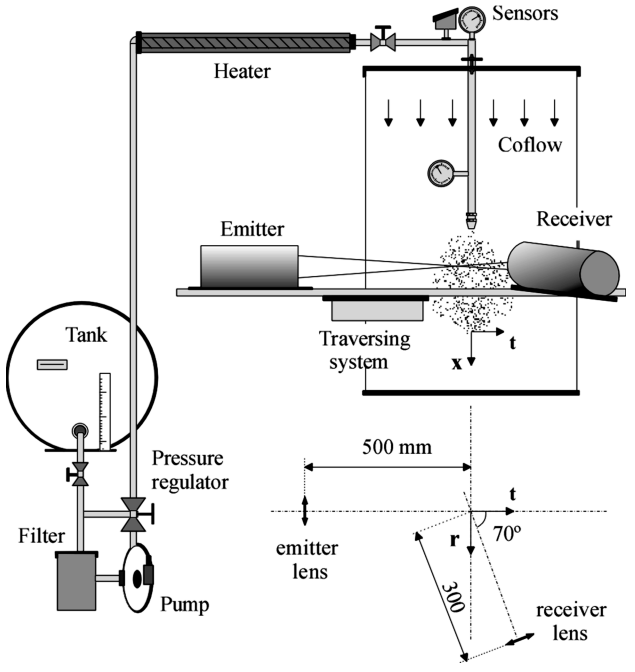

Fig. 1 Experimental setup.

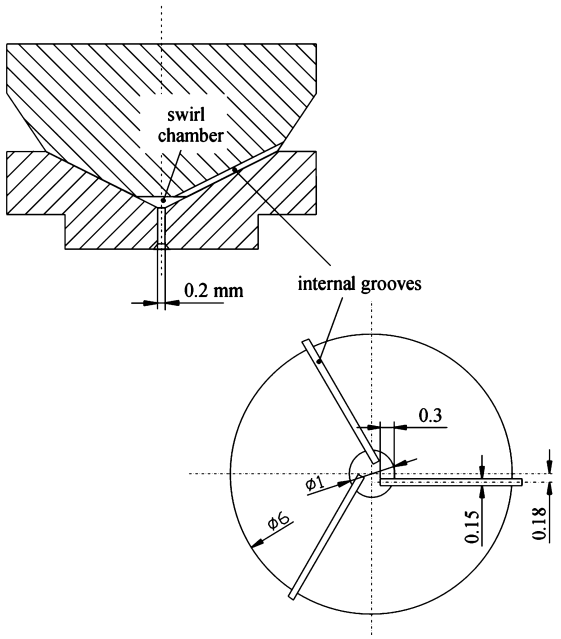

Fig. 2 Nozzle internal geometry.

A commercial pressure swirl nozzle of low flow rate and exit cone angle of 80 deg was used in this research. A schematic of the nozzle internal geometry is shown in Fig. 2. The pressurized liquid entered through three small grooves into the convergent swirl chamber where it was accelerated to the nozzle exit orifice of diameter 0.2 mm.

The injection conditions were controlled by a set of sensors. Temperature was fixed at 95°C and three different injection pressures were tested: 12, 16, and 20 bar.

Sprays developed inside a transparent chamber 340 mm square. An exhaust system provided a surrounding airflow into the chamber. The mean velocity of the coflow was 0.15 m/s. An auxiliary equipment was used to generate a very fine aerosol of water-glycerine mixture ($D_{10} = 3.4$ μm), which was added to the coflow allowing the continuous phase measurements by the PDPA technique. After atomization, the injected liquid was recovered for recycling.

A low-noise CCD and a stroboscopic light source of 0.5 μs pulse time were used to visualize the instantaneous disintegration of the emerging liquid film.

The spray measurements were carried out by means of a TSI-Aerometrics PDPA system which allowed us to simultaneously measure the drop size and two components of velocity. The receiving optics was placed to collect scattered light at 70 deg from the forward direction. At this angle the light scattering is dominated by first order of refraction and that due to reflection is a minimum. Thus, errors associated with trajectory ambiguities due to the Gaussian beam effect were reduced. Other geometrical settings were also tested but a not lineal relationship between phase shift and droplet diameter was detected. The beam separation was 40 mm and a transmissions lens with 500 mm of focal length was used. The focal length of the receiving optics was 300 mm. Both emitter and receiver were mounted on a traversing system controlled by a computer.

Spray Analysis Method

The near field of the sprays was characterized through the flow analysis at two axial stations located at 9 and 18 mm from the atomizer exit. The droplet diameter and both the axial and radial velocities, were measured every 2 mm in radial direction at each axial station using the PDPA system.

A typical validation rate profile along the spray field was the range of 85–95% for the velocities and 65–85% for the drop sizes. These validation rates reduced notably in the $P = 12$ bar case, at the nearest measurement station to the sheet breakup point. It should be noted

that the PDPA rejects signal from nonspherical droplets and does not take into account those due to multiple droplets in the probe volume.

The mean velocities were determined by averaging overall droplet size distribution at the respective locations. The Sauter mean diameter (SMD) was taken as characteristic parameter of the local droplet size distributions.

Furthermore, the following empirical expression [3] was chosen to evaluate the SMD of the oil sprays generated in the present work and to analyze the injection pressure effect:

$$\mathrm{SMD} = 2.25\sigma_l^{0.25}\mu_l^{0.25}\rho_l^{0.25}Q^{0.25}P^{-0.5}\rho_a^{-0.25} \tag{1}$$

The liquid volume flux was determined by the method based on the transit time of the droplets at the probe volume [12]. This method, which avoids errors due to the droplet trajectory through the probe volume, can be formulated as a particular case of the General Integral Method (GIM), such as it is proposed by Aisa et al. [13]. Nevertheless, the accuracy of droplet volume flux measurements depends on a perfect detection and size evaluation of all droplets crossing the probe volume and on the determination of the probe volume size itself. Other errors can also occur due to obscuration, either in the transmitting beams or in the receiving line of sight.

The volume flux corresponding to each droplet size class and all droplets were obtained by the following expressions [13]:

$$f_{V_i} = \frac{1}{\Delta t}\frac{\sum_{\forall kj} \mathrm{tt}_{kj}\cdot \boldsymbol{V}_{Dj}}{\mathrm{Vol}_i}\frac{\pi D_i^3}{6} \tag{2}$$

$$f_V = \sum_{i=1}^{N_{\mathrm{cl}}} f_{V_i} \tag{3}$$

Droplet volume fluxes were evaluated in axial direction. Under the hypothesis of axisymmetry, the total liquid flow rates at each measurement axial station, for each droplet size class and for all droplets, were calculated, respectively, as

$$F_{T_i} = \int_{S_T} f_{V_{xi}}\,\mathrm{d}s \tag{4}$$

$$F_T = \int_{S_T} f_{V_x}\,\mathrm{d}s \tag{5}$$

The spray boundary at each axial station was obtained from PDPA measurements, for the radial position where the data rate was less than 10 drops per minute.

The percentage of total liquid flow rate not measured was calculated as

$$\mathrm{def} = 100\left[1 - \frac{F_T}{Q}\right] \tag{6}$$

Finally, the percentage of cumulative liquid flow rate by droplet size classes was obtained as

$$\%F_{\mathrm{ac}} = 100\sum_{i=1}^{n}\frac{F_{T_i}}{F_T} \tag{7}$$

By constructing the cumulative distributions, it was possible to obtain the volume median diameter D_{V50} and the span parameter S, which were used to characterize the global droplet size distributions across the spray. The span is a dimensionless parameter calculated as

$$S = \frac{D_{V90} - D_{V10}}{D_{V50}} \tag{8}$$

where D_{V90} and D_{V10} are the smaller droplet diameters that include, respectively, 90 and 10% of the total liquid volumetric flow rate.

Table 2 Experimental data

Parameter	$P = 12$	$P = 16$	$P = 20$
Q, cm^3/s	0.662	0.777	0.854
$Re_o = \rho_l Q d_o / A_o \mu_l$	214	252	277
$C_D = Q/A_o\sqrt{2P/\rho_l}$	0.395	0.40	0.396

Spray analysis was carried out plotting variables evolution profiles on the dimensionless radial coordinate r^*. This coordinate was obtained as

$$r^* = \frac{r}{R_{50}} \tag{9}$$

where R_{50} is the radial position that includes 50% of the total liquid volumetric flow rate measured at each axial station. It can be interpreted as the radial mean spread of the spray.

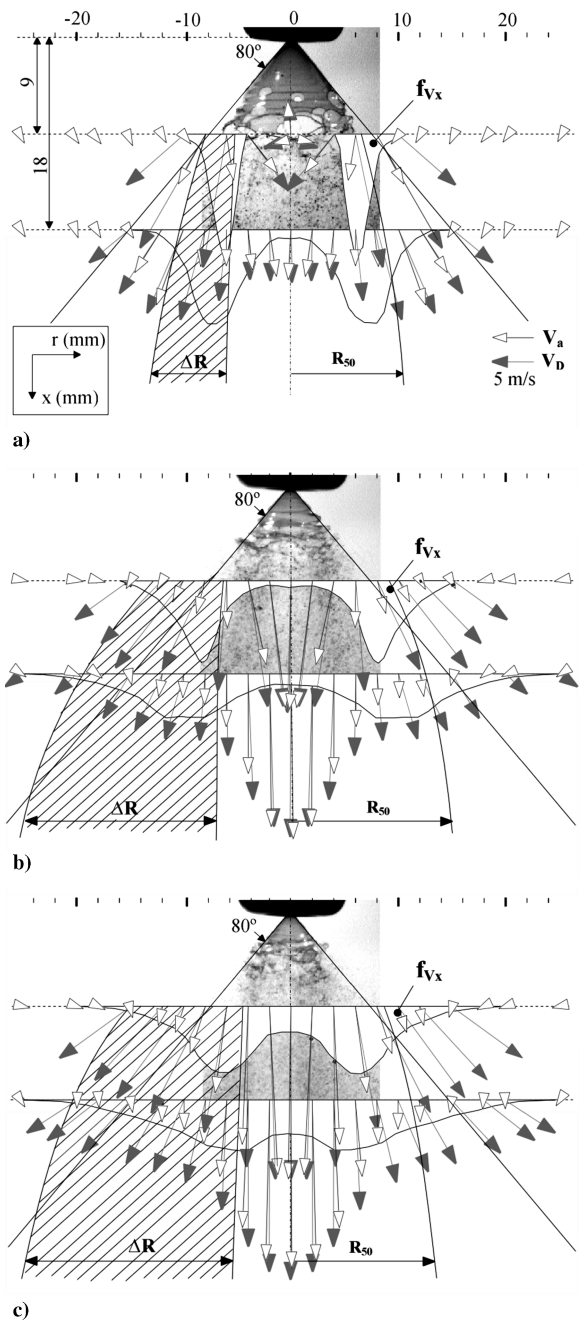

Fig. 3 Near-field spray structures. a) $P = 12$ bar, b) $P = 16$ bar, c) $P = 20$ bar.

Table 3 Liquid volumetric flow rate deficits, %

	Regime 1	Regime 2	
	$P = 12$	$P = 16$	$P = 20$
$x = 9$ mm	67.9	34.4	35.9
$x = 18$ mm	29.4	20.3	23.7

Table 4 Droplet Weber numbers[a]

	Regime 1	Regime 2	
	$P = 12$	$P = 16$	$P = 20$
$We_D = \rho_a V_{\text{rel}}^2 D/\sigma_1$	0.183	0.203	0.372

[a]Maxima values obtained at $x = 18$ mm.

Table 5 Entrained airflow rates, l/s

	Regime 1	Regime 2	
	$P = 12$	$P = 16$	$P = 20$
$x = 9$ mm	0.355	1.52	2.28
$x = 18$ mm	1.57	2.33	2.82

In a similar way, the characteristic radii R_{10} and R_{90}, which include, respectively, 10 and 90% of the total liquid flow rate at each axial station, were defined. Hence, the spray spatial dispersion parameter was obtained as follows:

$$\Delta R = R_{90} - R_{10} \tag{10}$$

The characterization of the continuous phase and subsequent determination of the air velocity fields was performed analyzing the signals of the smallest droplets (minor of 5 μm) which can supposedly follow the instantaneous changes in gas velocity.

The entrained airflow rate was calculated by integrating the local axial air velocities across the spray, such as shows the following expression:

$$F_{Ta} = \int_{S_T} V_{ax}\,\mathrm{d}s \tag{11}$$

Air mass flow rate balances were checked in several cylindrical control volumes to validate the continuous phase measurements. Average errors of 8% were obtained between incoming and outgoing airflow rates to the control volumes.

Experimental Results

The liquid volumetric flow rates injected through the atomizer were measured at each tested injection pressure. The Reynolds numbers at the exit orifice, Re_o, and the nozzle discharge coefficient, C_D, were also calculated. Values are summarized in the Table 2.

According to the regular performance of pressure atomizers, Q and Re_o increase as the pressure does. Seeing that the cone angle and the discharge coefficient acquired stable values at the tested pressure range, it was considered that the nozzle was working in its stable zone [14].

In Fig. 3, the images of the sheet instantaneous disintegration and the resulting near-field spray structures are presented for the three injection pressures studied. The mean velocity maps of the two phases (liquid and air) and the profiles of droplet axial volume flux, f_{V_x}, at each axial measurement station are plotted for the three cases. It is also shown the axial evolution of the radial mean spread parameter, R_{50}, and the radial dispersion of droplets, ΔR, which defines the spray zone where the liquid flow rate is mainly concentrated (dashed region in Fig. 3).

In each case it is observed that the emerging flow forms a conical sheet of angle 80 deg at the atomizer exit. According to the dominant sheet disrupting mechanisms, two distinct atomization regimes, named 1 and 2, were obtained as the injection pressure increases. In regime 1, at the pressure of 12 bar, the tulip-shaped sheet breaks by the growth of perforations mainly. In regime 2, at 16 and 20 bar, the diverging conical-shaped sheet breaks by the wave growth process. As the pressure increases, an intensification of the wave motion on the sheet surface and a reduction of the breakup length are produced.

The hollow cone structure of the sprays is remarked by the axial volume flux profiles, particularly at the closer axial location to the sheet breakup point. The liquid flow rates are initially concentrated in

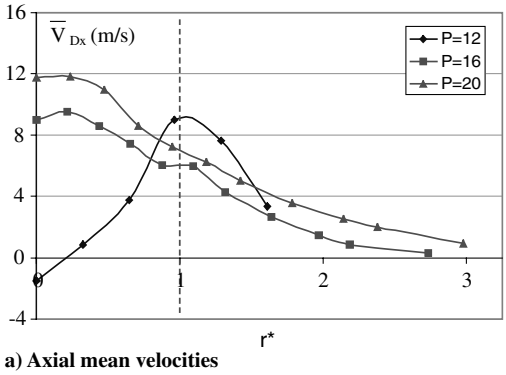

a) Axial mean velocities

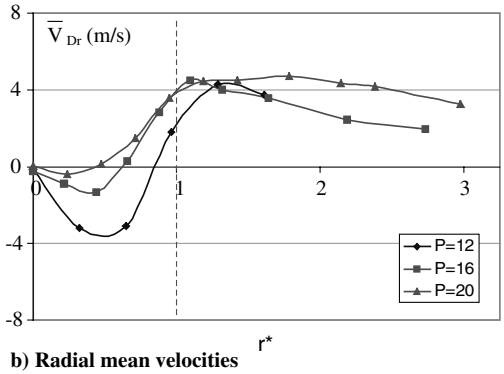

b) Radial mean velocities

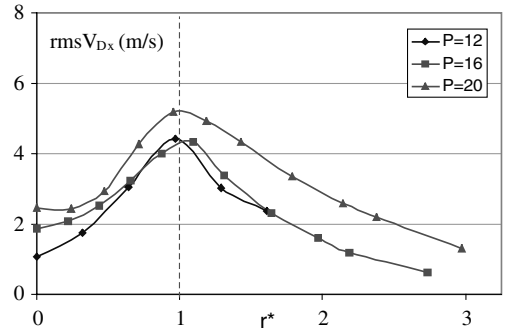

c) Axial rms velocities

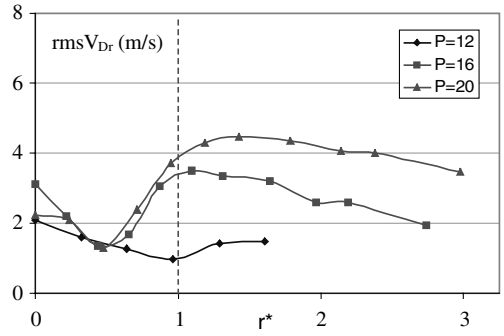

d) Radial rms velocities

Fig. 4 Profiles of mean and rms droplet velocity. Axial position: 9 mm.

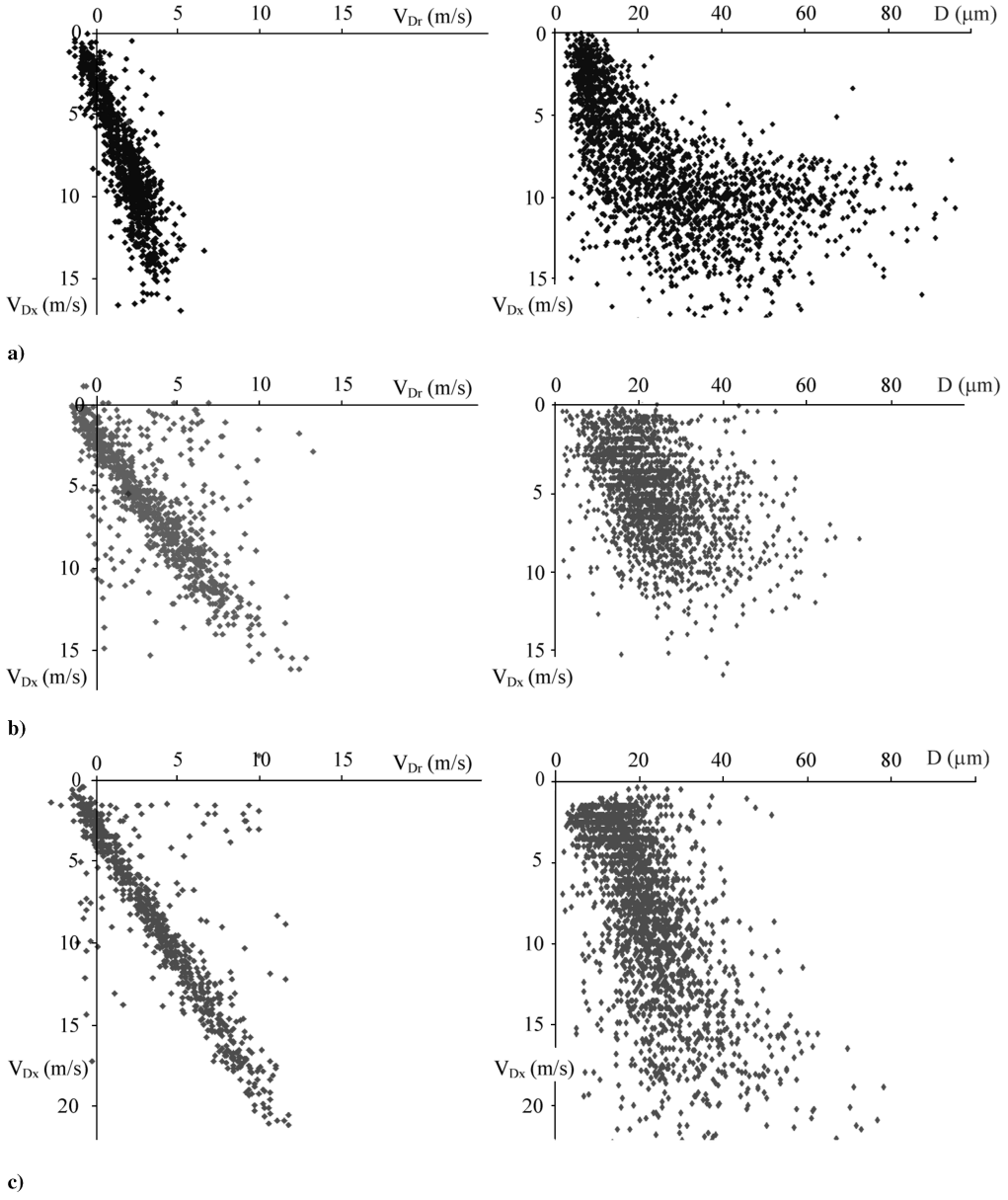

Fig. 5 Vertexes of the droplet velocity vectors (left). Droplet size–axial velocity correlations (right). Axial station: 9 mm. Radial position: $r^* = 1$. Cases: a) $P = 12$ bar, b) $P = 16$ bar, c) $P = 20$ bar.

a small region of annular cross section with the highest volume fluxes around the R_{50} position.

As the sprays develop, some phenomena like the droplet transport into the spray core by the incoming air and the droplet inertial classification cause the spatial redistribution of the liquid flow rate. Hence, the droplet radial dispersion increases downstream generating more uniform profiles of the axial volume flux. It is noted that the spray of regime 1 spreads out quite less than those of regime 2. As a consequence, the cross-transversal area of the spray is clearly more reduced.

The liquid flow rate deficits were calculated at each axial station from Eq. (6). As shown in Table 3, a significant deviation between the injected and measured liquid volumetric flow rates is obtained. The averaged deficit is 24% at 18 mm from the nozzle exit, similar to that obtained for other researchers [15]. As it was expected, higher deficits were obtained at the axial station of 9 mm, especially at $P = 12$ bar, where more difficulties in measuring were found due to the high liquid density.

The continuous phase velocity maps show that the surrounding air flows into the spray. The interaction between the incoming air and the dispersed phase gives rise to the smallest droplets transport towards the spray core. As a consequence, the dispersed and continuous phase velocities are practically coupled at this region. In regime 2 sprays, a high velocity central air jet is generated. However, in the 12 bar case, a vortex zone behind the leading edge of the conical sheet is observed due to the breakup proximity.

High relative mean velocities between phases are measured around the spray densest region and towards the spray periphery. Droplets will quickly decelerate downstream in the slower moving air by the strong momentum exchange. Nevertheless, phenomena as droplet deformation and secondary disintegration are found not significant due to the low values of the droplet Weber numbers (Table 4) obtained in the experiment.

The entrained airflow rates, obtained from Eq. (11), are summarized in Table 5 for the two axial measurement stations.

In all cases, the entrained airflow rates increase as the sprays develop. A bigger entrainment is noted for the regime 2 sprays, which present larger radial dispersion and higher axial air velocities than that of regime 1

Droplet Velocities

In Fig. 4, the profiles of mean and rms droplet velocity at the axial position of 9 mm are plotted using the r^* coordinate.

The liquid sheet breakup length and the effect of the air entrainment have a notable influence on the profiles of the droplet axial mean velocity (Fig. 4a). At $P = 12$ bar, where a very long liquid sheet is generated, the hollow cone structure of the spray is clearly perceptible, with a peak of axial velocity at $r^* = 1$. The axial mean velocity decays quickly and becomes negative at the axis due to the presence of the vortex zone.

On the other hand, in $P = 16$ and $P = 20$ bar cases, the transport of small droplets by the incoming air, generates the highest axial velocities at the central zone of the spray. The $P = 16$ bar profile forms a plateau around $r^* = 1$ due to the initial structure of the injected liquid.

Radial mean velocities (Fig. 4b) have negative values at $r^* < 1$ as a result of the smallest droplets motion toward the spray axis. The spray generated at $P = 12$ bar shows the widest negative zone with the highest velocity modules. This is due to the proximity of the sheet disintegration zone where the central air jet is initiated (see Fig. 3).

The axial rms velocity profiles (Fig. 4c) show the maximum around $r^* = 1$. These high droplet velocity fluctuations, located at the highest volume flux zone, were also observed by other researchers [11] and can be attributed to the high droplet size-velocity correlation resulting from the drag forces. Nevertheless, the effects of the sheet disintegration process, which involves the liquid instability mechanisms, should be more investigated.

Figure 5 shows the correlation between droplet size and their axial velocity component for a number of droplets moving at the local position of $r^* = 1$. Although we can note a positive size-velocity correlation, it is particularly significant the strong velocity fluctuation exhibited for each droplet size.

The vertexes of the velocity vectors are also represented in Fig. 5. For all cases, we can observe the strong correlation of the droplet velocity components and the high dispersion of velocity modules. In the $P = 12$ bar case, the axial velocity is clearly dominant, so the radial rms droplet velocities (Fig. 4d) reduces notably.

According to the classic kinetic theory of gases, the collision rate between droplets can be related to their own relative velocity [9]. Therefore, high collision rates are expected at the densest regions of the sprays. It is also noted (Fig. 5) that the relative velocity between droplets increases substantially at $P = 20$ bar, so higher inertia collisions will be produced in this case.

Droplet Sizes

The radial evolution of the Sauter mean diameter at 9 and 18 mm from the nozzle exit is shown in Fig. 6.

Profiles in regime 2 show the typical trend observed for hollow cone sprays, where the Sauter mean diameter increases progressively in radial direction. The smaller droplets are collected at the spray core transported by the continuous phase, whereas the larger droplets move to the spray edge, relatively unperturbed, according to a process of droplet inertial classification.

For regime 1, the proximity of the sheet breakup point to the axial distance of 9 mm generates a maximum of SMD at $r^* = 1$. Downstream, at 18 mm, the profiles of Sauter mean diameter reveal substantially bigger local droplet sizes than those measured for the regime 2. This significant decrease in atomization quality can also be observed in Fig. 7, where the number size distributions, at the local position of $r^* = 1$, are plotted.

It should be noted that the pressure increase tends to form a local bimodal size distribution. The significant increase of small droplets for higher pressures is believed to be the result of the increase of satellite droplets generation by collision phenomena.

This idea is supported by the fact that the rate of small droplets, produced after a collision, is higher as the relative velocities of the colliding droplets increase [8], and this occurs when the injection pressure is higher (see Fig. 5).

The presence of small droplets could be due to the secondary atomization process, as it is appointed in other investigations [16]. However, the low Weber numbers of the droplets generated in this experiment (see Table 4) do not suggests this possibility. Rüger et al. [9] assumed that this is a result of the Gaussian beam effect in the PDA measurements, but this problem was practically removed in the related work due to the selected optical configuration of the PDA.

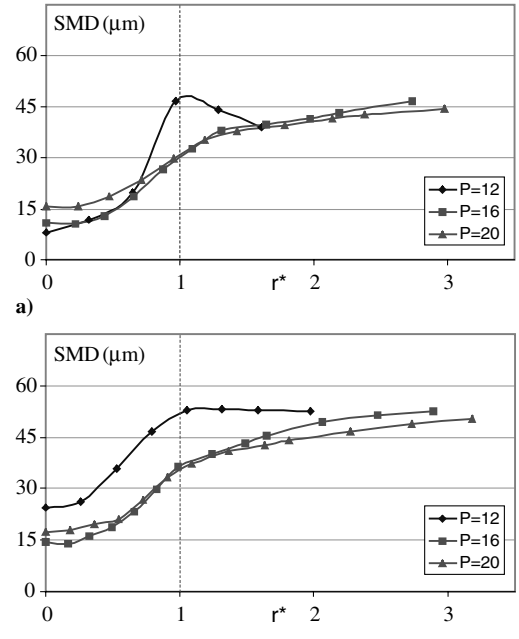

Fig. 6 SMD profiles. Axial positions: a) 9 mm, b) 18 mm.

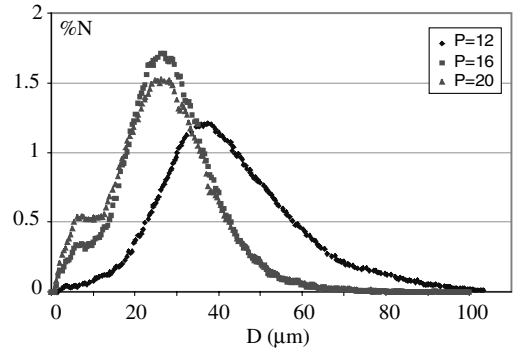

Fig. 7 Number size distributions. Axial station: 18 mm; radial location: $r^* = 1$.

The Sauter mean diameters of the droplet size distributions presented in Fig. 7 and those evaluated by the empirical expression of Eq. (1), proposed by Lefebvre [3], are listed in Table 6.

According to the expression, SMD progressively reduces as pressure increases. However, this trend was not recorded in these experimental measurements. A strong reduction of SMD is obtained as the regime change occurs but a light variation is only detected within regime 2. It can be deduced that the expression does not take account the effects of the sheet breakup mechanisms. Other essential consideration that does not appear in this type of empirical expressions is the lack of uniformity of the droplet size distribution along the spray.

Droplet Volume Fluxes

The evolution of droplet axial volume fluxes for each tested injection pressure was already presented in Fig. 3. In Fig. 8 the axial

Table 6 Sauter mean diameters, μm

	Regime 1	Regime 2	
	$P = 12$	$P = 16$	$P = 20$
SMD (Lefebvre [3])	46.1	41.5	37.9
SMD ($r^* = 1$)	52.1	36.5	35.7

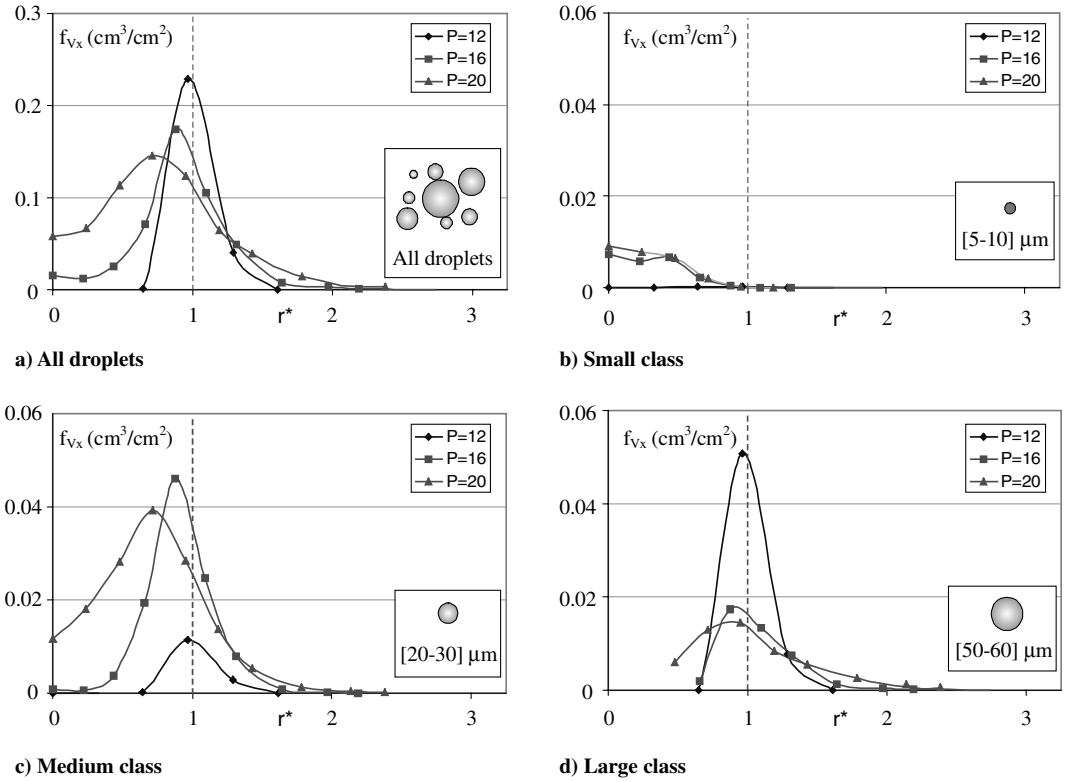

Fig. 8 Droplet axial volume flux profiles. Axial position: 9 mm.

volume fluxes at the axial location of 9 mm are plotted for all droplets and for three different droplet size classes that were named small, medium, and large. The small class included droplet diameters from 5 to 10 μm, the medium class, diameters from 20 to 30 μm, and the large class, diameters from 50 to 60 μm.

The typical hollow cone structure of the flow generated by a PSN is observed for the all droplets axial volume flux profiles (Fig. 8a), with low values at the spray axis and a maximum around $r^* = 1$. As the pressure increases, the maximum axial volume flux decreases due to progressive spatial distribution of the liquid droplets.

The small size class, concentrated at the spray center, only presents significant values of axial volume flux for the regime 2 (Fig. 8b). The hollow cone configuration of the sprays can also be perceived for the profiles of the medium and large droplet size classes (Figs. 8c and 8d). The medium class shows the highest axial volume flux values for the regime 2, whereas the large class shows the highest values for the regime 1, in coincidence with the droplet size distributions presented previously.

Cumulative Liquid Flow Rates

The cumulative liquid flow rate distributions at each axial station are plotted in Fig. 9 for the three injection pressures. These distributions show that a clearly finer spray is obtained for the atomization regime 2, and thus that the growth of surface waves is a more efficient liquid sheet breakup mechanism.

The statistical parameters of the cumulative distributions are listed in Table 7. D_{V50} reduces notably when pressure increases from 12 to 16 bar. The droplet size dispersion, evaluated through the span parameter, increases due mainly to the D_{V50} reduction.

Within regime 2, very small variations of D_{V50} and S are obtained as the pressure increases. These results do not agree with the common idea that a pressure increase leads to finer droplet distributions. However, it is according to theoretical predictions of the sheet disintegration process [17] that found a rather constant value of the droplet mean diameter for high injection pressure values. When pressure increases, two phenomena operate simultaneously with opposite effects. If the increasing liquid velocity enhances the destabilizing effects of the aerodynamic forces and reduces the population of large droplets, the disintegration occurs sooner and thereby with a thicker liquid sheet.

In all cases, we observe that the droplet mean diameter increases when the spray develops. Taking into account the high droplet collision rates that were predicted at the densest regions of the spray, it is considered that the coalescing collisions generate this evolution. Nevertheless, the probability of the different collision outcomes should be object of a more detailed study.

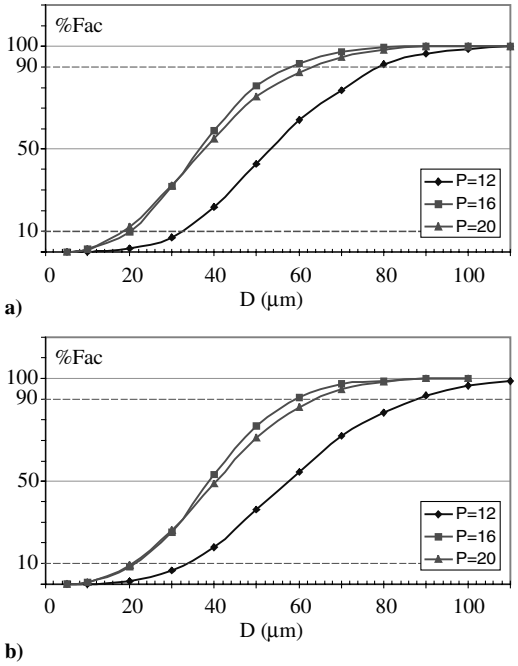

Fig. 9 Cumulative liquid flow rate distributions. Axial positions: a) 9 mm, b) 18 mm.

Table 7 Statistical parameters of distribution

		Regime 1	Regime 2	
		$P = 12$	$P = 16$	$P = 20$
$x = 9$	D_{V50}, μm	53.2	36.8	37.5
	S	0.86	1.04	1.18
$x = 18$	D_{V50}, μm	57.2	38.9	40
	S	0.94	0.98	1.09

Conclusions

Hollow cone pressure swirl sprays developing in a slow moving air were investigated using experimental techniques. The spray near field was analyzed at three different cases, which included two distinct sheet atomization regimes: perforations and surface wave instabilities.

All sprays showed the typical hollow cone structure of the injected liquid. The smallest droplets, transported by the entrained air, concentrated around the central zone. Wide drop size distributions were obtained toward the spray periphery and a continuous increase of the droplet mean diameter was measured in the radial direction. The parameter of spray radial mean spread was located near the position of maximum axial volume flux (spray densest region). A high dispersion of droplet velocity modules was detected at this region predicting high droplet collision rates. As a consequence of the coalescing collisions, the droplet mean size increased in axial direction.

When perforated-sheet changes to wavy-sheet disintegration, a notably finer spray with a higher radial dispersion was obtained. The entrained airflow rate showed a significant increase with higher axial velocities at the central zone. The air entrainment process notably affected to the droplet mean velocity profiles.

The sprays resulting of wavy conical sheets showed quite similar droplet mean sizes, according to theoretical predictions. It was observed the trend to form local bimodal drop size distributions at the densest region when injection pressure increases. The possible causes appointed in previous research works, as secondary atomization or the Gaussian beam effect, were rejected due to the experimental conditions. The increase of small droplets was attributed to the formation of satellite droplets for higher inertia collisions.

References

[1] Yule, A. J., and Chinn, J. J., "The Internal Flow and Exit Conditions of Pressure Swirl Atomizers," *Atomization and Sprays*, Vol. 10, No. 2, 2000, pp. 121–146.

[2] Inamura, T., Tamura, H., and Sakamoto, H., "Characteristics of Liquid Film and Spray Injected from Swirl Coaxial Injector," *Journal of Propulsion and Power*, Vol. 19, No. 4, 2003, pp. 632–639.

[3] Lefebvre, A. H., *Atomization and Sprays*, Hemisphere, New York, 1989.

[4] Ramamurthi, K., and Tharakan, T. J., "Flow Transition in Swirled Liquid Sheets," *AIAA Journal*, Vol. 36, No. 3, March 199, pp. 420–427.

[5] Chung, I. P., and Presser, C., "Fluid Property Effects on Sheet Disintegration of a Simplex Pressure-Swirl Atomizer," *Journal of Propulsion and Power*, Vol. 17, No. 1, 2001, pp. 212–216.

[6] Sommerfeld, M., "Analysis of Isothermal and Evaporating Turbulent Sprays by Phase-Doppler Anemometry and Numerical Calculations," *2nd International Symposium of Turbulence, Heat and Mass Transfer*, Delft Univ. Press, Delft, The Netherlands, 1997, pp. 55–68.

[7] Schelling, J., and Reh, L., "Influence of Atomiser Design and Coaxial Gas Velocity on Gas Entrainment into Sprays," *Chemical Engineering and Processing*, Vol. 38, No. 4, 1999, pp. 383–393.

[8] Qian, J., and Law, C. K., "Regimes of Coalescence and Separation in Droplet Collision," *Journal of Fluid Mechanics*, Vol. 331, 1997, pp. 59–80.

[9] Rüger, M., Hohmann, S., Sommerfeld, M., and Kohnen, G., "Euler/Lagrange Calculations of Turbulent Sprays: The Effect of Droplet Collisions and Coalescence," *Atomization and Sprays*, Vol. 10, No. 1, 2000, pp. 47–81.

[10] Feikema, D. A., Eskridge, R., and Hutt, J. J., "Structure of Nonevaporating Swirl Injector Spray," *Atomization and Sprays*, Vol. 7, No. 1, 1997, pp. 77–95.

[11] Lai, W. H., Wang, M. R., and Huang, D. Y., "Turbulence Modulation in a Simplex Spray," *ICLASS-1997*, edited by C. H. Lee, Begell House, New York, 1997, pp. 409–416.

[12] Zhu, J. Y., Rudoff, R. C., Bachalo, E. J., and Bachalo, W. D., "Number Density and Mass Flux Measurements Using the Phase Doppler Particle Analyzer in Reacting and Non-Reacting Swirling Flows," AIAA Paper 93-0361, Jan. 1993.

[13] Aísa, L., García, J. A., Cerecedo, L. M., García, I., and Calvo, E., "Particle Concentration and Local Mass Flux Measurements in Two Phase Flows with PDA. Application to a Study on the Dispersion of Spherical Particles in a Turbulent Air Jet," *International Journal of Multiphase Flow*, Vol. 28, No. 2, 2002, pp. 301–324.

[14] Dupoy, D., Florès, B., Lisiecki, D., and Dumouchel, C., "Behaviour of Swirl Atomizers of Small Dimensions," *ICLASS-1994*, edited by A. J. Yule and C. Dumouchel, Begell House, New York, 1994, pp. 121–129.

[15] Domnick, J., "Some Comments Concerning the State-of-the-Art of Phase Doppler Anemometry Applied to Liquid Sprays," *Proceedings of the 13th International Conference on Liquid Atomization and Spray Systems (ILASS-Europe '97)*, ENEL Pisa, Florence, Italy, 1997, pp. 134–140.

[16] Dumouchel, C., and Sindayihebura, D., "Drop Size Distribution Characteristics of Sprays Produced by Swirl Atomizers of Small Dimensions," *Proceedings of the 14th International Conference on Liquid Atomization and Spray Systems (ILASS-Europe '98)*, edited by A. J. Yule, UMIST, Manchester, England, U.K., 1998, pp. 236–242.

[17] Cousin, J., Yoon, S. J., and Dumouchel, C., "Coupling of Classical Linear Theory and Maximum Entropy Formalism for Prediction of Drop Size Distribution in Sprays: Application to Pressure-Swirl Atomizers," *Atomization and Sprays*, Vol. 6, No. 5, 1996, pp. 601–622.

J. Oefelein
Associate Editor